Electrostatic waves around a magnetopause reconnection diffusion region and their associations with whistler and lower-hybrid waves

Shan Wang[1*], Daniel B. Graham[2], Xin An[3], Li Li[1], Qiu-Gang Zong[1], Xu-Zhi Zhou[1], Wen-Ya Li[4], and Zhi-Yang Liu[1]

[1]Institute of Space Physics and Applied Technology, Peking University, Beijing, China 100871

[2]Swedish Institute of Space Physics, Uppsala SE-75121, Sweden

[3]Department of Earth, Planetary, and Space Sciences, University of California, Los Angeles, California, USA, 90095

[1]State Key Laboratory of Space Weather, National Space Science Center, Chinese Academy of Sciences, Beijing, China, 100190

*coralwang90@gmail.com

Key points

- Oblique electrostatic waves occur with but likely not due to nongyrotropic electron beams in the magnetospheric side EDR
- Parallel electron beam-mode waves are modulated by whistler near the current sheet mid-plane, by driving beams through Landau resonance
- Electron beam-mode and cyclotron waves are modulated by lower-hybrid waves near separatrices, with beam and loss cone distributions

Abstract

We investigate electrostatic waves in a magnetopause reconnection diffusion region event. In the electron diffusion region on the magnetospheric side, an oblique electrostatic wave is observed. The local distribution exhibits fast non-gyrotropic electron beams with drifts comparable to the electron thermal speed, but the wave has a much lower phase speed. Response of ions and possible cold electrons may contribute to wave excitation. Near the current sheet mid-plane, parallel electron beam-mode waves are modulated by whistler waves. In the separatrix region, parallel waves associated with field-aligned electron beams and perpendicular electron cyclotron waves with loss cone distributions exhibit modulation frequencies in the lower-hybrid wave frequency range. We infer that lower-hybrid waves scatter electrons to produce beams and alter loss cones to modulate electrostatic waves. The results advance our understanding about the regimes and mechanisms of electrostatic waves in reconnection and their coupling with lower-frequency waves.

Plain Language Summary

Magnetic reconnection is an important energy dissipation process at the Earth's dayside magnetopause. In its central region, plasmas deviate from the thermal equilibrium and form structured distribution functions, which excite plasma waves. We investigate high-frequency electrostatic waves in an event, where the waves are associated with electron beam – plasma interaction or anisotropy of distribution functions. A rarely presented case of an oblique wave is observed, and the wave property is unexpected compared to local distribution features. We further find that electrostatic waves are driven and modulated by lower-frequency waves, as the latter alters the particle distribution functions. The results help us understand how various processes couple with each other to achieve the energy dissipation.

1. Introduction

Magnetic reconnection explosively converts energies from electromagnetic fields to plasmas. Highly structured non-Maxwellian distributions are created in reconnection, which can be unstable to a variety of plasma waves that further interact with particles, so waves may be potential pathways of achieving the energy dissipation in reconnection.

Quasi-electrostatic waves at the electron Debye length (D_e) scale are ubiquitous plasma phenomena, and the responsible excitation mechanisms are often associated with beam-plasma interactions, e.g., an electron beam drifting with respect to background electrons and ions. For one-dimensional electrostatic waves in unmagnetized (or field-aligned) plasmas with multiple populations, the dispersion relation is (modified from eq. (8.4.18) in Gurnett and Bhattacharjee, 2005):

$$1 - \frac{1}{2}\sum_s \frac{\omega_{ps}^2}{k^2 v_{ts}^2} Z'(\zeta^s) = 0 \quad (1)$$

where for each species s, ω_{ps} is the plasma frequency, $v_{ts} = \sqrt{2T_s/m_s}$ is the thermal speed, Z' is the derivative of the plasma dispersion function, $\zeta^s = (\omega - kV_s)/(kv_{ts})$, and V_s is the bulk velocity. For populations with $|\zeta^s| \gg 1$, the contribution to eq. (1) is of the cold beam type $\sim \frac{\omega_{ps}^2}{(\omega - kV_s)^2}$ or with thermal corrections such as in Langmuir waves $\sim \frac{\omega_{ps}^2}{(\omega - kV_s)^2}\left[1 + \frac{3k^2 v_{ts}^2}{2(\omega - kV_s)^2}\right]$. For $|\zeta^s| \ll 1$, the term is $\sim \frac{\omega_{ps}^2}{3k^2 v_{ts}^2}$, such as for hot electrons in ion/electron acoustic waves. The Langmuir wave has $\omega \geq \omega_{pe}$, and it tends to be the dominant mode if the beam is weak and suprathermal (Omura et al., 1996; Lu et al., 2005; An et al., 2019). The beam or

acoustic modes often have $\omega < \omega_{pe}$, though occasions exist in the Earth's magnetosphere regime where $\omega > \omega_{pe}$ (Fuselier et al., 1985). When the electron beam speed is comparable to the background electron thermal speed ($V_{beam} \sim v_{te,bg}$), it tends to excite instabilities through electron-electron interactions, and the resulting wave has high frequencies ($\omega \gg \omega_{pi}$) and high phase speeds (V_{ph}) comparable to $v_{te,bg}$; a slow electron beam ($V_{beam} \ll v_{te,bg}$) tends to excite waves through electron-ion interactions, and the resulting Buneman-like or ion acoustic-like waves have low frequencies ($\omega \lesssim \omega_{pi}$) and low V_{ph} (Norgren et al., 2015; Graham et al., 2016). Such quasi-parallel waves are commonly observed in reconnection regions (e.g., Khotyaintsev et al., 2019 and references therein), which may trap particles and thermalize distributions (e.g., Khotyaintsev et al., 2020). For quasi-perpendicular waves, non-gyrotropic electron distributions in the electron diffusion region (EDR) may excite upper hybrid waves (e.g., Graham et al., 2017; Burch et al., 2019) and electron Bernstein waves (e.g., Li et al., 2020), which may alter the distributions, pressure and potentially the reconnection electric field (Dokgo et al., 2020a, b; Li et al., 2020, 2021).

Waves at higher frequencies may be modulated by those at lower-frequencies, a way to cause energy transfer across scales. For example, inside the magnetosphere, ultra-low-frequency waves may modulate electromagnetic-ion-cyclotron waves (e.g., Liu et al., 2022), whistler and electron cyclotron harmonic (ECH) waves (e.g., Zhang et al., 2019); kinetic Alfven waves may modulate time domain structures around

injection fronts (An et al., 2021). Whistler waves with oblique propagations may produce parallel beams that drive Langmuir or electron acoustic waves (An et al., 2019), observed in magnetopause reconnection (Li et al., 2018) as well as other environments like the radiation belt (Li et al., 2017) and foreshock (Wang et al., 2020).

During magnetopause reconnection, electrostatic waves are commonly observed and they are capable of penetrating to the central EDR region, e.g., statistical results by Wilder et al (2019). However, there still lacks a systematic picture about what regimes of electrostatic waves are applicable in each reconnection sub-region, and whether and how they are coupled with other waves. Using burst-mode measurements of the Magnetosphere Multiscale (MMS) mission (detailed data descriptions in the Supplementary Information), we find rich electrostatic waves around an EDR event at magnetopause. We analyze the wave properties and corresponding plasma conditions, trying to advance the comprehension of the questions above.

2. Observations

2.1 Overview of the context and waves in the event

The event was on 26 February, 2018 (Figure 1). MMS crossed the magnetopause reconnection current sheet with B_L reversals (Figure 1b), where $B_L>0$ indicates the magnetospheric side. The LMN coordinate is determined by MVA during 09:52:04.4-09:52:07.1 UT, where L=[-0.3561, -0.2697, 0.8946], M=[-0.2353, -0.9007,

-0.3652], N=[0.9043, -0.3406, 0.2593] GSM. Overall the spacecraft was in a reconnection exhaust with large $V_{iL}>0$ (Figure 1c) and dense magnetosheath-origin electrons dominate the spectrogram (Figure 1a). Around 09:52:08 UT, a strong positive V_{eM} (Figure 1d) is observed. The associated V_{eL} reversal indicates a possible crossing from the +L to -L sides of an X-line. As shown later, MMS1 observed non-gyrotropic electron beams with $v_{||}<0$ at 08:52:08.1 UT (Figure 2i) while MMS3 observed intense electron beams with $v_{||}>0$ around 09:52:08.5 - 09:52:08.7 UT (Figure 4g), further supporting the encounter of an EDR (embedded in a primary reconnection outflow) with a break of the magnetic field topology and electron demagnetization.

The event has rich wave activities as seen in the FFT power spectra of electric (Figure 1e) and magnetic fields (Figure 1g). Lower-hybrid waves (LHWs) are observed with electromagnetic fluctuations mainly below the lower-hybrid frequency (f_{lh}), with occasions extending much above f_{lh}. The wave power is strongest where B_L has large positive values and V_{eM} is strong, indicating the close vicinity to the density gradient near the magnetospheric separatrix/boundary of the EDR current sheet. LHWs are possibly also excited near the magnetosheath side separatrix with large negative B_L, and the wave fields penetrate to the current sheet mid-plane with small $|B_L|$, where the wave is weaker (e.g., around 09:51:30 and 09:52:30 UT). In this study, we refer to whistler waves as the narrow-band enhancement slightly below $f_{ce}/2$ (marked in Figure 1g) close to the current sheet mid-plane.

Our focus is the electrostatic wave mainly above $f_{ce}/2$ with the power enhancements marked by a purple oval. On the magnetospheric side ($B_L>0$, e.g., 09:52:10-09:52:30 UT), quasi-parallel waves dominate with $|E_{||}|^2/|E|^2$ close to unity (Figure 1f). On the magnetosheath side ($B_L<0$, e.g., 09:51:40-09:52:05 UT), bands of perpendicular waves ($|E_{||}|^2/|E|^2 \sim 0$) are present slightly above f_{ce}, co-existing with parallel waves.

2.2 An isolated oblique wave packet in the EDR

We first zoom in to look at waves in the EDR (Figure 2). Appreciable wave enhancements occur around the ion plasma frequency (f_{pi}) mainly in $E_{||}$ (Figures 2c-2e). One encounter of oblique waves stands out (marked in Figures 2c-2d) with comparable $E_{||}$ and $E_{\perp}$, indicated by the greenish color in $|E_{||}|^2/|E|^2$ (Figure 2e) and the field-aligned coordinate (FAC) waveform (Figure 2f) that further indicates a linear polarization. Based on the 1D FFT spectrum of fields between dashed vertical lines in Figure 2f, the strong wave power expands at 1~15 f_{ce} (f_{ce}=313 Hz) or 0.4-5.9 f_{pi} (f_{pi}=802 Hz, marked in Figure 2g). The wave propagation direction is determined to be $\hat{\boldsymbol{k}} = [-0.8464, 0.3464, 0.4000]LMN$ by the maximum variance direction of electric fields above f_{ce}, $\theta_{kB} = 125°$. The wave number is estimated by the wavelet coherence analysis of probe-to-satellite potentials at a pair of the spin-plane probes (Graham et al., 2016), oriented 44° from $\boldsymbol{k}$. The resulting dispersion relation is shown as dots in Figure 2h, where colors represent the wave power. k is mainly at 0.01-0.02 m^{-1}, corresponding to kD_e=0.17-0.34, where D_e~17 m. The presented frequencies have been down-shifted to the ion-rest-frame by a small amount of 50-100 Hz. V_{ph} for

158 individual frequency channels are in the range of 200-1000 km/s, and the solid
159 magenta line in Figure 2h is a linear fit of *f-k* that requires crossing the origin, which
160 gives a representative V_{ph}=662 km/s. Thus, V_{ph} is mostly greater than the v_{ti} ~ 330
161 km/s and much smaller than v_{te}~ 5370 km/s (82eV).
162
163 The electron distribution partly sampled in the wave interval
164 (09:52:08.088-09:52:08.118 UT) exhibits a non-gyrotropic population (asymmetric
165 along $v_{\perp 1}$ (bulk $V_{e\perp}$ direction)) with a $v_{||}$<0 drift. It indicates a location around the
166 magnetospheric boundary of the EDR current layer where magnetosheath-origin
167 electrons are not fully magnetized and move away from the X-line (e.g., Burch et al.,
168 2016; Chen et al., 2016a). Additional background electrons exist, and the extension to
169 large $v_{||}$>0 is consistent with electrons from the magnetospheric inflow region with
170 parallel heating (e.g., Le et al., 2017; Wang et al., 2017). The non-gyrotropic electrons
171 provide a possible energy source of exciting electrostatic waves. However, we find
172 that the bulk $\boldsymbol{V}_{e\perp}$ is almost perpendicular to $\boldsymbol{k}_{\perp}$ with an angle of 74°, inconsistent
173 with the expectation that $\boldsymbol{k}_{\perp}$ should be aligned with $\boldsymbol{V}_{e\perp}$.
174
175 In order to further test whether the local distribution with non-gyrotropic electron
176 beams can excite the observed waves, we model the distribution and apply a linear
177 instability analysis using the dispersion solver 'BO' (Xie, 2019). The electron
178 distribution is modeled with 5 populations shown in Figure 2j (velocity ranges used
179 for fitting individual populations are marked in Figure 2i, details in the

Supplementary Information). Populations 1&2 may be treated as a background, and populations 3-5 together form a non-gyrotropic beam. Calculating the partial moments, the ratio of relative drift ($v_{d,12}$) between the background (1&2) and the beam (3-5) to the parallel thermal speed of the background ($v_{t,345}$) is 1.12 (greater than unity), and the relative drift is 159° from the magnetic field direction. Ions are approximately at rest, and $\omega_{pe}/\omega_{ce} = 80$. The linear instability analysis predicts a maximum growth rate at $\theta_{kB} = 155°$, along which positive growth occurs at $\mathrm{kD_e} = 0.15 - 1.30$, $\omega_r/\omega_{pi} = 3.5 - 38.0$ (solid curves in Figure 2k). The maximum growth is at $\mathrm{kD_e} = 0.62$, $\omega_r/\omega_{pi} = 28$, with V_{ph}=1.5$v_{t,345}$ close to the beam drift speed. The high frequency and V_{ph} demonstrate that the instability is mainly associated with the electron-electron interactions.

We tentatively conclude that the observed wave is not directly related to the free energy provided by the local fast non-gyrotropic electron beam. The predicted electron beam/acoustic instability is roughly along the beam direction, at frequencies much higher than f_{pi} and V_{ph} comparable to v_{te}. In contrast, the observed wave is only up to a few f_{pi} with a rather small V_{ph}, and $\boldsymbol{k}_\perp$ is almost perpendicular to $\boldsymbol{V}_{e\perp}$.

The source of the observed wave is inconclusive, but it has a couple of indications. The measurement of low-energy electrons near V_{ph} of a few hundred km/s is missing; however, MMS observed cold ions in the magnetospheric inflow region about 20 min later (not shown). These cold ions and electrons may enter the reconnection region,

which may excite ion/electron acoustic waves (e.g., Ergun et al., 2016). In fact, V_{ph} is close to the acoustic speed $c_s = \sqrt{(3T_i + T_e)/m_i}$~624 km/s.

2.3 Parallel electron beam mode waves in whistler

A series of electrostatic waves are present and modulated in the whistler wave in the vicinity of the current sheet mid-plane (B_L~0, Figure 3). Whistler occurs at slightly below $f_{ce}/2$ (Figure 3c), associated with the perpendicular anisotropy of energized magnetosheath electrons (seen in Figure 3j) slightly downstream of the central EDR (Wang et al., 2022). We select whistler waves as bins in FFT spectrograms that have magnetic field powers >10 times of the background noise level, degree of polarization > 0.7, and ellipticity > 0.5 (using the spectral analysis (Samson and Olson, 1980)). The parallel Poynting flux for the identified whistler wave is positive (Figure 3d), indicating a propagation away from the mid-plane toward the magnetosheath side. Enhancements of high-frequency electrostatic wave powers (Figures 3b-3c) lie in $f_{pi}<f<f_{pe}$, with the peak power sometimes slightly below f_{pe} such as around 09:52:09.15-09:52:09.40 UT and sometimes just above f_{pi} such as around 09:52:09.6 UT (the peak power ~3000 Hz is well resolved). The zoom-in plots (Figures 3g-3i) show that the electrostatic waves are mainly along $E_{||}$ and the occurrence is clearly modulated by whistler. For example, eight wave packets occur during an interval of 0.05s from 09:52:09.32 to 09:52:09.37 UT, corresponding to a modulation frequency of 160 Hz, equal to the whistler frequency. Figure 3i further shows that the electrostatic wave occurs at the negative $E_{||}$ phase of whistler, a feature consistent with the secondary wave produced by an oblique whistler with $V_{ph||}>0$ (e.g., Li et al.,

2018; An et al., 2019). Electrons with velocities close to $V_{ph||}$ can be trapped by whistler through nonlinear Landau resonance. The trapped population gets accelerated toward larger $v_{||}$ during the negative $E_{||}$ phase, forming a beam to trigger secondary instabilities.

The above scenario is more quantitatively supported by wave properties and electron distribution features. For selected whistler bins in Figure 3d, we estimate $V_{ph||}$ using $\frac{|E|}{|B|cos\theta_{kB}}$ (magenta dots in Figure 3e) with the median values at each time shown with a black curve, where the calculated θ_{kB} is around 30°. The values are 3000-5000 km/s, slightly larger than those from the cold plasma dispersion relation ($V_{ph||} = \sqrt{\frac{\omega(\Omega_{ce}cos\theta_{kB}-\omega)}{\omega_{pe}^2}}$) of 2000-2500 km/s (blue diamonds). The electron $v_{||}$ spectrogram (Figure 3f) exhibits holes between background and beams around the estimated median values of $V_{ph||}$ at 09:52:09.2-09:52:09.4 UT, also seen in the 2D distribution (Figure 3j). Beam speeds oscillate, which indicates possible modulations by whistler, though data resolution is not sufficient to fully resolve the whistler-frequency signature.

In the magnetopause reconnection context, electrostatic waves driven and modulated by whistler have been reported (Li et al., 2018). They mainly discussed an event in the magnetospheric separatrix region, where whistler originates from anisotropy of hot magnetospheric electrons. The $V_{ph||}$ is around 2×10^4 km/s above local v_{te}, such that the dominant secondary electrostatic wave is Langmuir wave (An et al., 2019). Our

event, as well as an event mentioned in Li et al. (2018), occurs in the vicinity of the current sheet mid-plane, where whistler arises from the anisotropy of energized magnetosheath-origin electrons in the reconnection exhaust. The corresponding $V_{ph||}$ (a few thousand km/s) is comparable to v_{te}, which theoretically excites electron beam/acoustic mode waves at a fraction of f_{pe} (An et al., 2019). Li et al. (2018) observed waves slightly below f_{pe}; our event has occasions of waves slightly below f_{pe} and also at lower frequencies just above f_{pi}.

2.4 Electron beam modes and cyclotron waves in LHWs

Modulations of electrostatic waves are also found inside LHWs. Figure 4 (left) shows MMS3 observations in the magnetospheric side separatrix region around the density gradient (Figure 4a). LHWs are present mainly below f_{lh}, and extend to higher frequencies in the most intense intervals near 09:52:07 UT (Figures 4e and 4f). We find that separate high-frequency electrostatic waves mainly along $E_{||}$ are present, seen in the waveform that co-exist with $E_{\perp}$ of LHWs (Figure 4c). Their power spectrum is extracted by plotting $\left|E_{\parallel}\right|^2 - |E_{\perp}|^2$ (Figure 4d), mainly at $f_{pi}<f<f_{pe}$. The electron $v_{||}$ spectrogram (Figure 4g) exhibits beams. Persistent intense beams at $v_{||}>0$ like those around 09:52:06.7-09:52:07.0 UT, with an example distribution in Figure 4h, are possible magnetosheath electrons moving away from the X-line as the outflow. Later in the lower-density region, the less intense beams repeatedly change directions, also seen in 2D distributions (Figures 4i-4k).

It has been reported that large-amplitude $E_{||}$ exist in LHWs (e.g., Ergun et al., 2019). We further analyze that high-frequency $E_{||}$ waves may be modulated by LHWs, readily suggested by wave power enhancements that are discrete in time. The recurrence frequency is quantified with the waveform filtered at 0.3-33 kHz during 09:52:06.7-09:52:07.1UT inside the most intense LHWs (Figure 4h). $E_{||}$ wave packets are present with amplitudes up to ~60 mV/m. We identify the envelops of the wave packets (black curve) and extract their maxima (black dots, required to be >2 mV/m). The reciprocal of intervals between the adjacent maxima are calculated to estimate the recurrence frequency. With 40 identified maxima, the median recurrence frequency is 131 Hz, and the 25% and 75% quartiles are 73 Hz and 164 Hz, respectively. The values well lie in the range of the high-frequency part of LHWs, indicating modulations of $E_{||}$ waves by LHWs. LHWs typically have quasi-perpendicular propagations with non-zero $k_{||}$, and the associated $E_{||}$ may modulate and resonate with electrons (e.g., Cairns and McMillan, 2005; Graham et al., 2019; Wang et al., 2021; Ng et al., 2023). Therefore, LHWs may modify the distribution near their $V_{ph||}$ and excite secondary parallel waves, in a similar way with whistlers. In addition, LHWs produce diffusion for plasmas across boundaries (e.g., Price et al., 2017; Le et al., 2017; Graham et al., 2022), where field-aligned beams can be produced (Le et al., 2018). We infer that electron beams with positive/negative $v_{||}$ (not necessarily near $V_{ph||}$ of LHWs) may be generated during the diffusion process, and the beams excite electrostatic waves.

LHW-modulated high-frequency waves are also observed in the magnetosheath separatrix region with large B_L<0 (Figure 4, right). Waveforms show high-frequency waves (Figure 4m) in the midst of LHWs (dominant fluctuations in Figure 4n). LHWs are mainly below f_{lh}~25 Hz (Figure 4q), while high-frequency waves are mainly above f_{ce} (Figure 4o-4p). High-frequency $E_{\perp}$ waves exhibit harmonic features, possibly ECH waves. ECHs have been reported in the magnetosheath separatrix region (Zhou et al., 2016). The FFT spectra of electric and magnetic fields for an example interval between vertical dashed lines are shown in Figures 4s-4t. The harmonics are right at integers of f_{ce} up to $6f_{ce}$ in electric fields, and one peak can be seen in magnetic fields at $1f_{ce}$, indicating a weak electromagnetic component. Additional broadband $E_{||}$ waves are present at higher frequencies than ECH and below f_{pe}. The electron distribution (Figure 4u) that covers the interval of this wave burst shows a loss cone feature (or perpendicular anisotropy) at $v_{||}$>0. The spacecraft was at +L side of the X-line at this time, so energetic electrons moving away from the X-line are at $v_{||}$<0, causing the asymmetry between field-aligned directions (Fuselier et al., 2013; Chen et al., 2016b). ECHs are likely excited by loss cone distributions.

ECH wave powers are modulated (Figure 4o): seven bursts show up during ~0.5s at 09:52:03.02-09:52:03.52 UT, corresponding to a modulation frequency of 14Hz in the LHW range. We further calculate the LHW potential in Figure 4r (method of Norgren et al. (2012)), which shows that ECH enhancements (marked by vertical dotted lines) tend to occur at the slopes of the potential, corresponding to peak wave electric fields

312 possibly driving electron vortices in LHWs (e.g., Ergun et al., 2019; Chen et al.,
313 2020). These gyro-scale potential structures may inflate/compress electron
314 distributions and generate non-gyrotropic features (e.g., Chen et al., 2020; Wang et al.,
315 2021). We infer that the LHW structures modify the loss cone electron distributions in
316 the magnetosheath separatrix region, possibly changing the phase-space gradient of
317 distributions, and modulate ECHs.
318
319 **3. Summary and Discussions**
320 Based on MMS observations of one magnetopause reconnection diffusion region
321 crossing, we identify widely presented electrostatic waves in different sub-regions.
322 We analyze the wave and plasma properties, and find their associations with
323 lower-frequency waves. The findings are summarized in Figure 1h.
324 (1) Inside the EDR on the magnetospheric side of the mid-plane, isolated waves are
325 observed, and one particular wave packet is highly oblique. The wave extends
326 from a fraction of to a few f_{pi}, with a low V_{ph} much smaller than the electron
327 thermal speed. Oblique electrostatic waves have been rarely discussed. Zhong et
328 al. (2021) showed one example downstream of the EDR within the ion diffusion
329 region (illustrated with a magenta word in Figure 1h). The diffusion region
330 provides a special environment of unmagnetized plasmas, which should be critical
331 for the presence of such oblique waves. In both Zhong et al. (2021) and the
332 present case, V_{ph} are low. It indicates that ions and/or cold
333 ionosphere/plasmaspheric electrons may play a role for the wave excitation, and

the mechanism needs to be further understood.

The electron distribution accompanied with the wave has a fast non-gyrotropic beam, expected to excite beam-mode waves at higher frequencies. It requires future work to understand whether and how such typical EDR electron distributions affect electrostatic instabilities.

(2) Parallel electron beam mode waves driven and modulated by whistler are observed in the vicinity of the mid-plane. Adding to Li et al. (2018), with their finding about the Langmuir wave in whistler near the magnetospheric separatrix (included in Figure 1h), we further complete the regimes of whistler and the associated secondary waves in the context of magnetopause reconnection.

(3) Analogous to the idea for whistler, we infer that LHWs can also modulate high-frequency waves. In LHWs near both magnetospheric and magnetosheath side separatrices, high-frequency wave powers are periodically enhanced with recurrence frequencies in the range of the LHW frequency. On the magnetospheric side, field-aligned electron beams that change directions over time are observed. We infer that LHWs may periodically scatter and produce these beams as they diffuse the density gradient, and the beams excite electron beam mode waves. On the magnetosheath side, ECHs tend to occur at the slopes of LHW potentials. We infer that LHWs modify the loss cone distribution in the separatrix region and modulate ECHs. The exact dynamics about LHW modulations still acquire a better understanding.

This event helps us step forward on building a map of waves in reconnection regions, learning about the applicable wave regimes and understanding the coupling of different processes in reconnection. We expect that more systematic and statistical studies of electrostatic waves in reconnection will help consolidate our understanding and solve the open questions.

Acknowledgements

SW thanks Dr. Hua-Sheng Xie for helpful discussions on linear instability analyses and thanks Dr. Chao Yue for suggestions on paper presentations. Research at PKU is supported by "The Fundamental Research Funds for the Central Universities, Peking University" No. 7100604293.

Data Availability

MMS data are available at https://lasp.colorado.edu/mms/sdc/public/. One can go to the tab of 'About the Data', 'Browse the SDC', and select data for specific satellites, e.g., 'mms1'.

References

An, X., Li, J., Bortnik, J., Decyk, V., Kletzing, C., & Hospodarsky, G. (2019). Unified view of nonlinear wave structures associated with whistler‐mode chorus.

Physical Review Letters, 122(4), 045101. https://doi.org/10.1103/PhysRevLett.122.045101

Burch, J. L., et al. (2016), Electron-scale measurements of magnetic reconnection in space, Science, 352(6290), 1189, doi:10.1126/science.aaf2939.

Burch, J. L., Dokgo, K., Hwang, K. J., Torbert, R. B., Graham, D. B., Webster, J. M., et al. (2019). High‐frequency wave generation in magnetotail reconnection: Linear dispersion analysis. Geophysical Research Letters, 46, 4089–4097. https://doi.org/10.1029/2019GL082471

Cairns, I. H., and B. F. McMillan (2005), Electron acceleration by lower hybrid waves in magnetic reconnection regions, Phys. Plasmas, 12, 102110, doi:10.1063/1.2080567.

Chen, L.-J., M. Hesse, S. Wang, N. Bessho, and W. Daughton (2016a), Electron energization and structure of the diffusion region during asymmetric reconnection, Geophys. Res. Lett., 43, 2405–2412, doi:10.1002/2016GL068243.

Chen, L.-J., et al. (2016), Electron energization and mixing observed by MMS in the vicinity of an electron diffusion region during magnetopause reconnection, Geophys. Res. Lett., 43, 6036–6043, doi:10.1002/2016GL069215.

Chen, L.-J., Wang, S., Le Contel, O., Rager, A., Hesse, M., Drake, J., et al. (2020). Lower-hybrid drift waves driving electron nongyrotropic heating and vortical flows in a magnetic reconnection layer. Physical Review Letters, 125, 025103. https://doi.org/10.1103/PhysRevLett.125.025103

Dokgo, K., Hwang, K.-J., Burch, J. L., Choi, E., Yoon, P. H., Sibeck, D. G., & Graham, D. B. (2019). High-frequency wave generation in magnetotail reconnection: Nonlinear harmonics of upper hybrid waves. Geophysical Research Letters, 46, 7873–7882. https://doi.org/10.1029/2019gl083361

Dokgo, K., Hwang, K.-J., Burch, J. L., Yoon, P. H., Graham, D. B., & Li, W. (2020a). High-frequency waves driven by agyrotropic electrons near the electron diffusion region. Geophysical Research Letters, 47(5), e2020GL087111. https://doi.org/10.1029/2020gl087111

Dokgo, K., Hwang, K.-J., Burch, J. L., Yoon, P. H., Graham, D. B., & Li, W. (2020b). The Effects of Upper-Hybrid Waves on Energy Dissipation in the Electron Diffusion Region. Geophysical Research Letters, 47(19), e2020GL089778. https://doi.org/10.1029/2020GL089778

Ergun, R., Holmes, J., Goodrich, K., Wilder, F., Stawarz, J., & Eriksson, S. (2016). Magnetospheric multiscale observations of large-amplitude, parallel, electrostatic waves associated with magnetic reconnection at the magnetopause. Geophysical Research Letters, 43(11), 5626–5634. https://doi.org/10.1002/2016GL068992

Ergun, R., Tucker, S., Westfall, J., Goodrich, K., Malaspina, D., & Summers, D. (2016). The axial double probe and fields signal processing for the MMS mission. Space Science Reviews, 199(1–4), 167–188.

Ergun, R. E., Hoilijoki, S., Ahmadi, N., Schwartz, S. J., Wilder, F. D., Drake, J. F., et al. (2019). Magnetic reconnection in three dimensions: Modeling and analysis of electromagnetic drift waves in the adjacent current sheet. Journal of Geophysical

420 Research: Space Physics, 124,10085 – 10103.
421 https://doi.org/10.1029/2019JA027275
422 Fuselier, S. A., Gurnett, D. A., and Fitzenreiter, R. J. (1985), The downshift of
423 electron plasma oscillations in the electron foreshock region, J. Geophys.
424 Res., 90(A5), 3935– 3946, doi:10.1029/JA090iA05p03935.
425 Fuselier, S. A., K. J. Trattner, and S. M. Petrinec (2011), Antiparallel and component
426 reconnection at the dayside magnetopause, J. Geophys. Res., 116, A10227,
427 doi:10.1029/2011JA016888.
428 Graham, D. B., Khotyaintsev, Y. V., Vaivads, A., & André, M. (2015). Electrostatic
429 solitary waves with distinct speeds associated with asymmetric reconnection.
430 Geophysical Research Letters, 42(2), 215–224.
431 https://doi.org/10.1002/2014GL062538
432 Graham, D. B., Khotyaintsev, Y. V., Vaivads, A., & Andre, M. (2016). Electrostatic
433 solitary waves and electrostatic waves at the magnetopause. Journal of
434 Geophysical Research: Space Physics, 121(4), 3069–3092.
435 https://doi.org/10.1002/2015JA021527
436 Graham, D. B., Khotyaintsev, Y. V., Vaivads, A., Norgren, C., André, M., Webster, J.
437 M., et al. (2017). Instability of agyrotropic electron beams near the electron
438 diffusion region. Physical Review Letters, 119, 025101.
439 https://doi.org/10.1103/PhysRevLett.119.025101
440 Graham, D. B., Khotyaintsev, Y. V., Norgren, C., Vaivads, A., André, M., Drake, J.
441 F., et al. (2019). Universality of lower hybrid waves at Earth's magnetopause.

442 Journal of Geophysical Research: Space Physics, 124, 8727 – 8760.
443 https://doi.org/10.1029/2019JA027155
444 Graham, D. B., Khotyaintsev, Y. V., André, M., Vaivads, A., Divin, A., Drake, J. F.,
445 et al. (2022). Direct observations of anomalous resistivity and diffusion in
446 collisionless plasma. Nature Communications, 13(1),
447 2954. https://doi.org/10.1038/s41467-022-30561-8
448 Gurnett, D. A. and Bhattacharjee, A. (2005), Chapter 8: Electrostatic waves in hot
449 unmagnetized plasma, in Introduction to plasma physics with space and
450 laboratory applications, Cambridge University Press, ISBN: 0521367301.
451 Jiang, K., Huang, S. Y., Yuan, Z. G., Sahraoui, F., Deng, X. H., Yu, X. D., et al.
452 (2019). The role of upper hybrid waves in the magnetotail reconnection electron
453 diffusion region. The Astrophysical Journal Letters, 881(2), L28.
454 https://doi.org/10.3847/2041-8213/ab36b9
455 Khotyaintsev, Y. V., Graham, D. B., Norgren, C., & Vaivads, A. (2019). Collisionless
456 magnetic reconnection and waves: Progress review. Frontiers in Astronomy and
457 Space Sciences, 6(70), 1–20. https://doi.org/10.3389/fspas.2019.00070
458 Khotyaintsev, Y. V., Graham, D. B., Steinvall, K., Alm, L., Vaivads, A., & Johlander,
459 A. (2020). Electron heating by debye-scale turbulencein guide-field reconnection.
460 Physical Review Letters, 124(4), 045101.
461 Le Contel, O., Leroy, P., Roux, A., Coillot, C., Alison, D., & Bouabdellah, A. (2016).
462 The search-coil magnetometer for mms. Space Science Reviews, 199(1–4), 257–
463 282.

Le, A., Daughton,W., Chen, L.-J., & Egedal, J. (2017). Enhanced electron mixing and heating in 3-d asymmetric reconnection at the earth's magnetopause. Geophysical Research Letters, 44, 2096–2104. https://doi.org/10.1002/2017GL072522

Li, J., Bortnik, J., Li, W., Thorne, R. M., Ma, Q., Chu, X., et al. (2017). Coherently modulated whistler mode waves simultaneously observed over unexpectedly large spatial scales. Journal of Geophysical Research: Space Physics, 122, 1871–1882. https://doi.org/10.1002/2016JA023706

Li, J., Bortnik, J., An, X., Li, W., Russell, C. T., Zhou, M., et al. (2018). Local excitation of whistler mode waves and associated Langmuir waves at dayside reconnection regions. Geophysical Research Letters, 45, 8793 – 8802. https://doi.org/10.1029/2018GL078287

Li, W. Y., Graham, D. B., Khotyaintsev, Y. V., Vaivads, A., André, M., Min, K., et al. (2020). Electron Bernstein waves driven by electron crescents near the electron diffusion region. Nature Communications, 11(1), 141. https://doi.org/10.1038/s41467-019-13920-w

Li, W.-Y., Khotyaintsev, Y. V., Tang, B.-B., Graham, D. B., Norgren, C., Vaivads, A., et al. (2021). Upper-hybrid waves driven by meandering electrons around magnetic reconnection X line. Geophysical Research Letters, 48, e2021GL093164. https://doi.org/10.1029/2021GL093164

Lindqvist, P.-A., Olsson, G., Torbert, R., King, B., Granoff, M., & Rau, D. (2016). The spin-plane double probe electric field instrument for mms. Space Science Reviews, 199(1–4), 137–165.

Liu, Z.-Y, Q.-G Zong, R. Rankin, H. Zhang, Y. F. Wang, X.-Z. Zhou, S.-Y. Fu, C. Yue, X.-Y Zhu, C. J. Pollock, S. A. Fuselier, and G. Le (2022), Simultaneous macroscale and microscale wave-ion interaction in near-earth space plasmas. Nat. Commun. 13, 5593. https://doi.org/10.1038/s41467-022-33298-6

Lu, Q., S. Wang, and X. Dou (2005), Electrostatic waves in an electron-beam plasma system, Phys. Plasmas, 12, 072903, https://doi.org/10.1063/1.1951367

Ng, J., J. Yoo, L.-J. Chen, N. Bessho, and H. Ji (2023), 3D simulation of lower-hybrid drift waves in strong guide field asymmetric reconnection in laboratory experiments, Phys. Plasmas, 30, 042101, doi: 10.1063/5.0138278

Norgren, C., Vaivads, A., Khotyaintsev, Y. V., & Andre, M. (2012). Lower hybrid drift waves: Space observations. Physical Review Letters, 109, 55001. https://doi.org/10.1103/PhysRevLett.109.055001

Norgren, C., André, M., Graham, D., Khotyaintsev, Y. V., & Vaivads, A. (2015). Slow electron holes in multicomponent plasmas. Geophysical Research Letters, 42(18), 7264–7272. https://doi.org/10.1002/2015GL065390

Omura, Y., Matsumoto, H., Miyake, T., & Kojima, H. (1996). Electron beam instabilities as generation mechanism of electrostatic solitary waves in the magnetotail. Journal of Geophysical Research, 101(A2), 2685–2697.

Pollock, C., Moore, T., Jacques, A., Burch, J., Gliese, U., & Saito, Y. (2016). Fast plasma investigation for magnetospheric multiscale. Space Science Reviews, 199(1–4), 331–406.

Price, L., Swisdak, M., Drake, J. F., Burch, J. L., Cassak, P. A., & Ergun, R. E. (2017). Turbulence in three-dimensional simulations of magnetopause reconnection. Journal of Geophysical Research: Space Physics, 122, 11,086–11,099. https://doi.org/10.1002/2017JA024227

Russell, C., Anderson, B., Baumjohann, W., Bromund, K., Dearborn, D., & Fischer, D. (2016). The magnetospheric multiscale magnetometers. Space Science Reviews, 199(1–4), 189–256.

Samson, J. C., & Olson, J. V. (1980). Some comments on the descriptions of the polarization states of waves. Geophysical Journal International, 61(1), 115–129.

Wang, S., Chen, L. J., Hesse, M., Wilson, L. B., Bessho, N., Gershman, D. J., et al. (2017). Parallel electron heating in the magnetospheric inflow region. Geophysical Research Letters, 44, 4384 – 4392. https://doi.org/10.1002/2017GL073404

Wang, S., Chen, L.-J., Ng, J., Bessho, N., Le, G., Fung, S. F., et al. (2020). A case study of nonresonant mode 3-s ULF waves observed by MMS. Journal of Geophysical Research: Space Physics, 125, e2020JA028557. https://doi.org/10.1029/2020JA028557

Wang, S., Chen, L.-J., Bessho, N., Ng, J., Hesse, M., Graham, D. B., et al. (2021). Lower-hybrid wave structures and interactions with electrons observed in magnetotail reconnection diffusion regions: Simulation dataset, https://doi.org/10.5281/zenodo.5651243

Wang, S., Bessho, N., Graham, D. B., Le Contel, O., Wilder, F. D., Khotyaintsev, Y. V., et al. (2022). Whistler waves associated with electron beams in magnetopause reconnection diffusion regions. Journal of Geophysical Research: Space Physics, 127, e2022JA030882. https://doi.org/10.1029/2022JA030882

Wilder, F. D., Ergun, R. E., Hoilijoki, S., Webster, J., Argall, M. R., Ahmadi, N., & Giles, B. L. (2019). A survey of plasma waves appearing near dayside magnetopause electron diffusion region events. Journal of Geophysical Research: Space Physics, 124(10), 7837–7849. https://doi.org/10.1029/2019JA027060

Xie, H. (2019). BO: A unified tool for plasma waves and instabilities analysis. Computer Physics Communications, 244, 343 – 371. https://doi.org/10.1016/j.cpc.2019.06.014

Zhang, X.-J., Chen, L., Artemyev, A. V., Angelopoulos, V., & Liu, X. (2019). Periodic excitation of chorus and ECH waves modulated by ultralow frequency compressions. Journal of Geophysical Research: Space Physics, 124, https://doi.org/10.1029/2019JA027201

Zhong, Z. H., Graham, D. B., Khotyaintsev, Y. V., Zhou, M., Le Contel, O., Tang, R. X., & Deng, X. H. (2021). Whistler and broadband electrostatic waves in the multiple X-line reconnection at the magnetopause. Geophysical Research Letters, 48, e2020GL091320. https://doi.org/10.1029/2020GL091320

Zhou, M., AshourAbdalla, M., Berchem, J., Walker, R. J., Liang, H., ElAlaoui, M., & Chandler, M. O. (2016). Observation of high-frequency electrostatic waves in the vicinity of the reconnection ion diffusion region by the spacecraft of the

magnetospheric multiscale (mms) mission. Geophysical Research Letters, 43(5), 4808–4815. https://doi.org/10.1002/2016GL069010

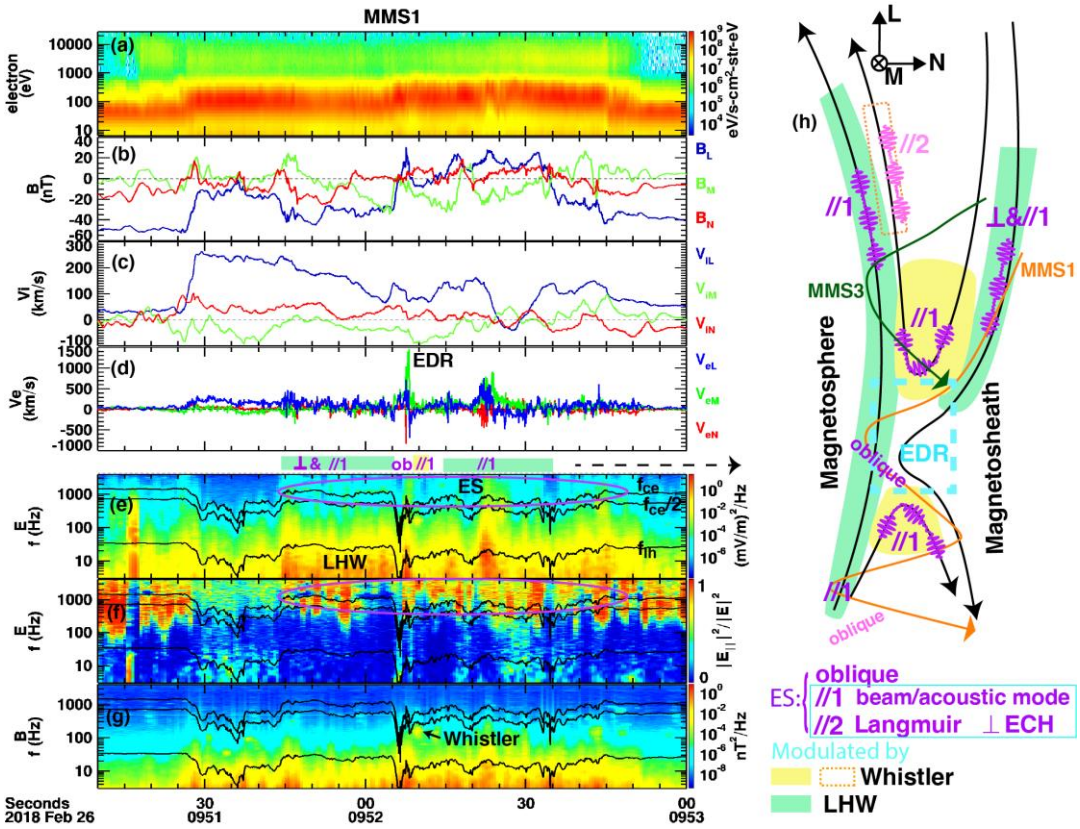

552

553 **Figure 1.** Overview of the event. (a) electron spectrogram; (b) ***B***; (c) $\boldsymbol{V_i}$; (d) $\boldsymbol{V_e}$; (e) ***E***

554 power spectrum; (f) $|E_{||}|^2/|E|^2$; (g) ***B*** power spectrum. (h) Illustrative summary of

555 electrostatic waves in magnetopause reconnection. Repeated wave packets indicate

556 modulations electrostatic waves by whistler or LHWs.

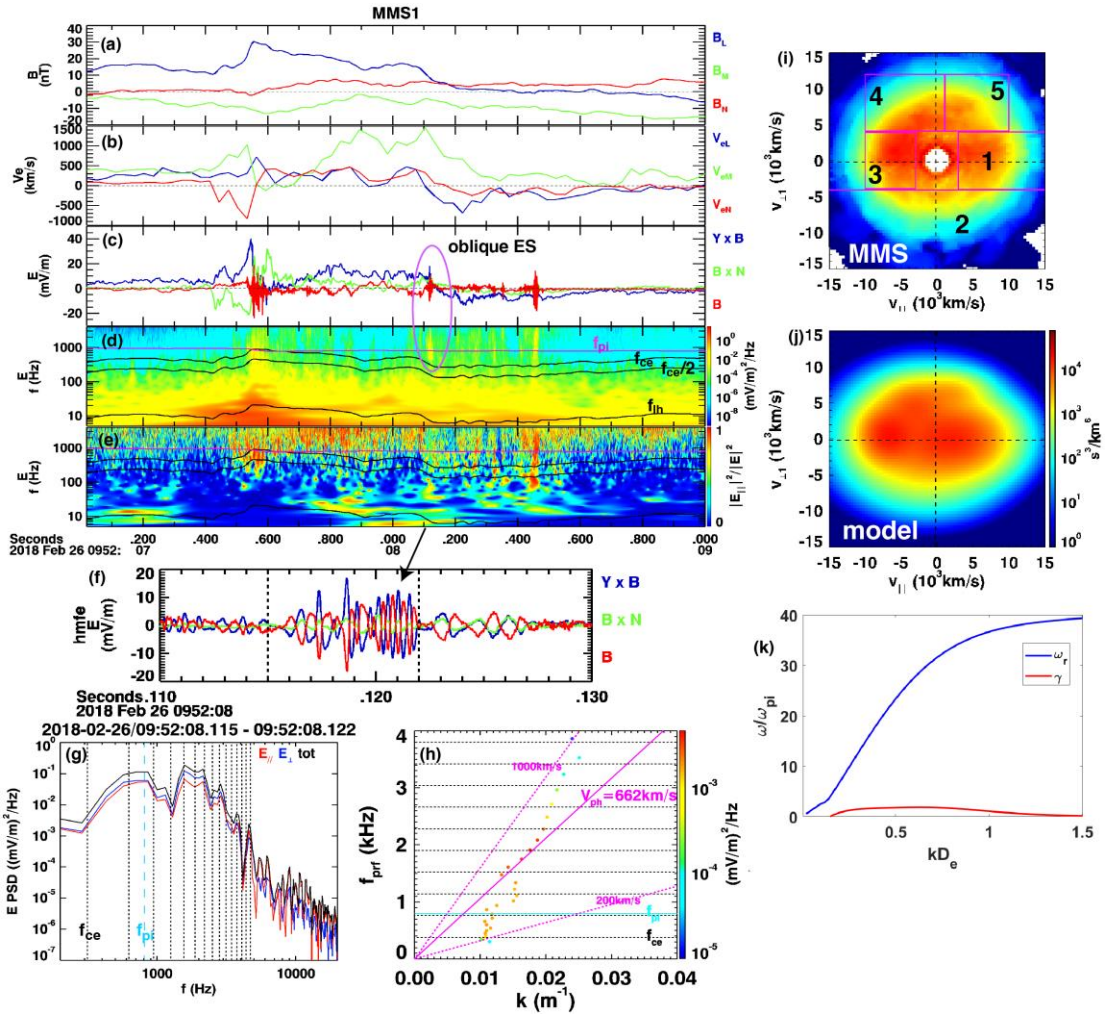

Figure 2. An isolated oblique wave in the EDR. (a) ***B***; (b) electron velocity showing large V_{eM} and V_{eL} reversal; (c) ***E*** in FAC; (d) ***E*** power spectrum; (e) $|E_{||}|^2/|E|^2$; (f) electric field waveform of the oblique wave; (g) FFT spectrum of the oblique wave; (h) deduced dispersion relation of the observed wave; (i)-(j) observed and modeled electron distribution at the wave; (k) dispersion relations for the instability analysis of the model distribution, which shows much higher frequencies than the observed wave.

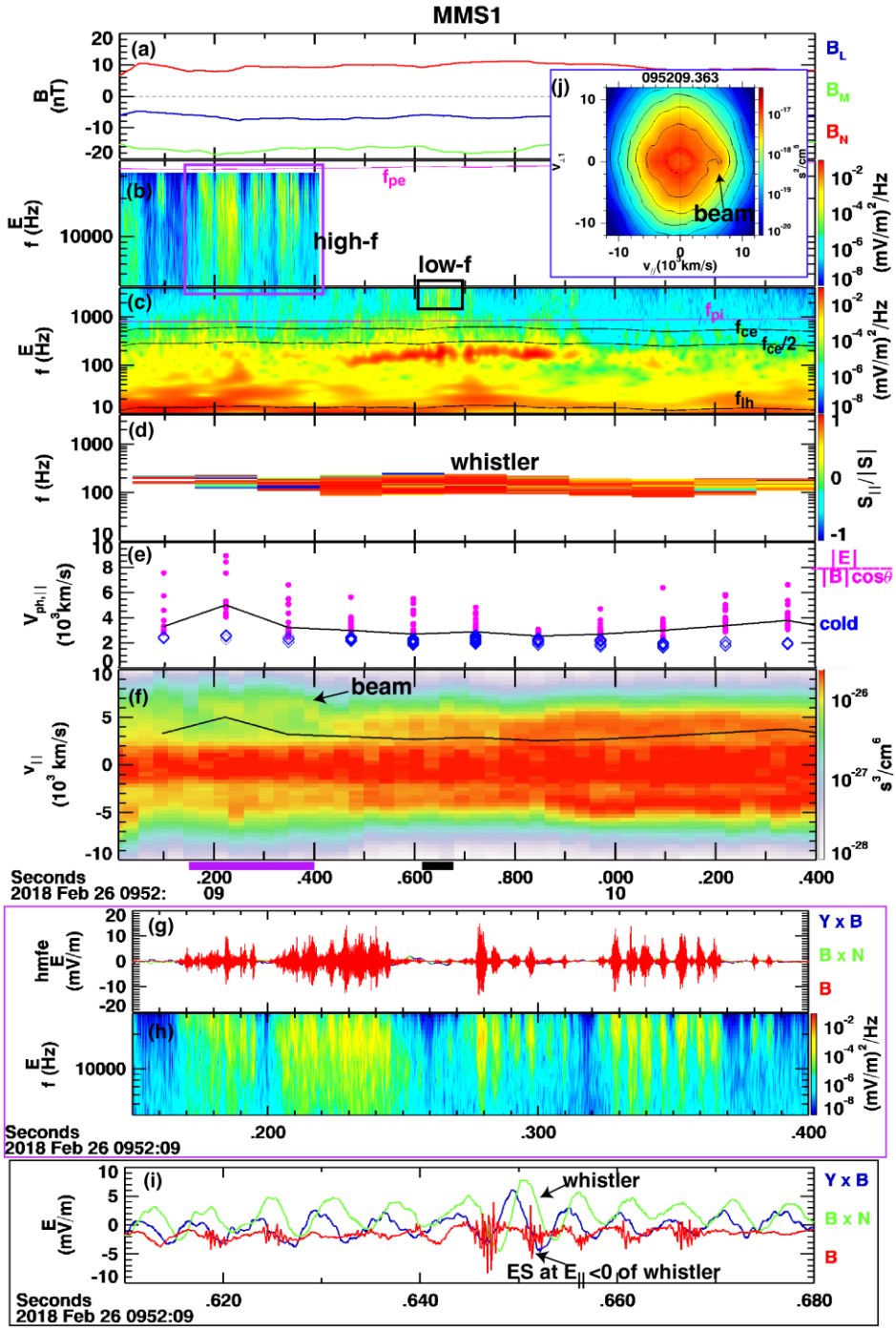

564

565 **Figure 3.** Parallel electrostatic waves (beam/acoustic mode below f_{pe}) modulated by
566 whistler waves near the current sheet mid-plane. (a) ***B***; (b)-(c) ***E*** power spectrum,
567 showing whistler slightly below $f_{ce}/2$ and electrostatic waves at $f_{pi}<f<f_{pe}$. (d) parallel
568 Poynting flux for selected whistler wave bins; (e) estimated parallel phase speed ($V_{ph||}$)
569 of whistler, magenta: $|E|/(|B|cos\theta_{kB})$, black: median of magenta dots, blue:
570 theoretical values in the cold plasma limit. (f) electron $v_{||}$ spectrogram, showing holes
571 near the whistler $V_{ph||}$ (black curve), also seen in the 2D distribution in (j). (g)-(h)
572 example waveform and power spectrum of modulated electrostatic waves slightly
573 below f_{pe}. (i) example waveform showing electrostatic waves slightly above f_{pi}
574 occurring at the negative $E_{||}$ phase of whistler.

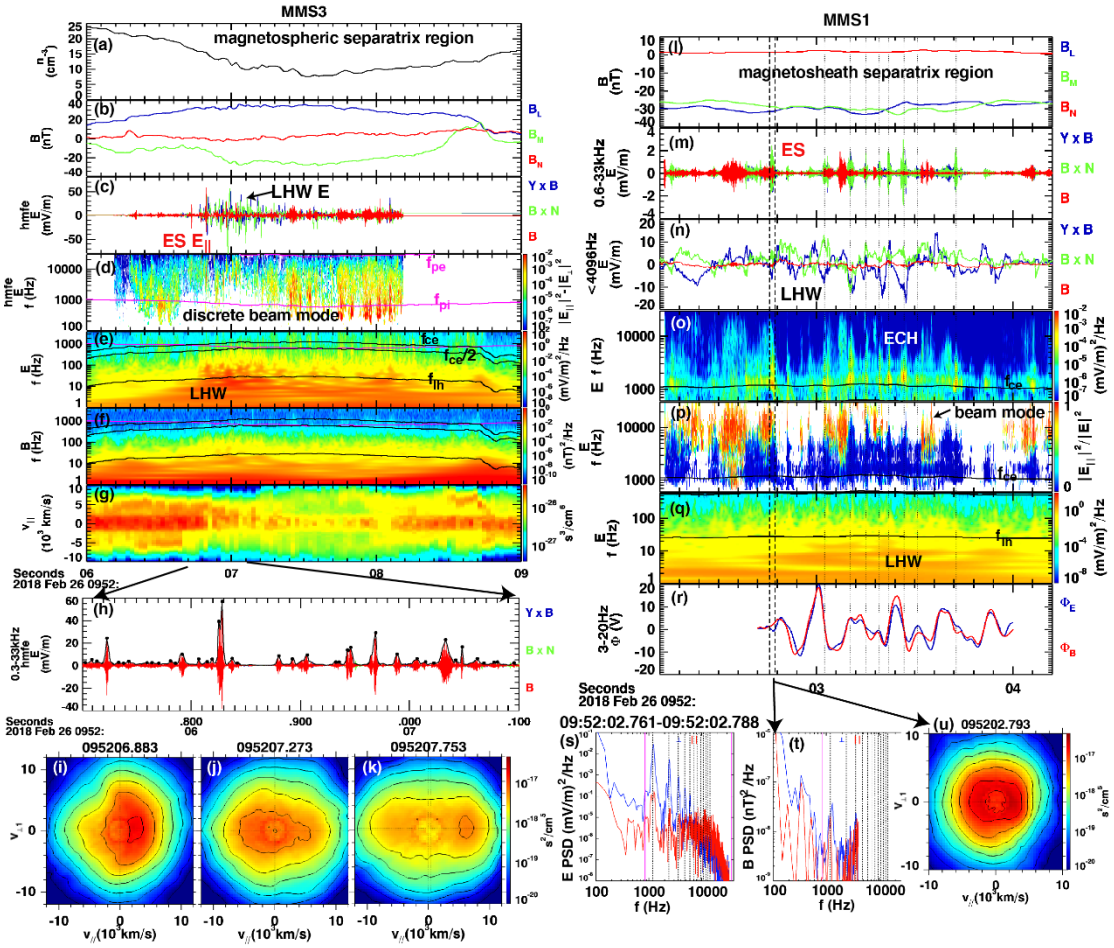

Figure 4. Left: parallel electrostatic waves modulated by lower-hybrid waves in the magnetospheric separatrix region. (a) electron density; (b) ***B***; (c) AC electric field; (d) power spectrum of $|E_{||}|^2 - |E_{\perp}|^2$ showing enhancements of parallel electrostatic waves; (e) ***E*** power spectrum at low frequencies showing lower-hybrid waves; (f) ***B*** power spectrum; (g) electron $v_{||}$ spectrogram; (h) filtered electric field waveform showing $E_{||}$ waves (red); black curve: envelop of the wave; black dots: extracted maxima of the envelops showing a recurrence rate in the lower-hybrid wave frequency range. (i)-(k) example electron distributions showing field-aligned beams with varying directions. Right: perpendicular ECH waves modulated by lower-hybrid waves in the magnetosheath separatrix region. (l) ***B***; (m)-(n) high- and low-frequency electric field waveforms; (o)-(p) ***E*** power spectrum and $|E_{||}|^2/|E|^2$ showing modulated perpendicular ECH and additional parallel waves. (q) low-frequency electric field power spectrum showing lower-hybrid waves. (r) lower-hybrid wave potential, with ECH enhancements at potential slopes. (s)-(t) electric and magnetic field FFT spectra for the interval between vertical dashed lines in (l)-(r). The corresponding electron distribution exhibits a loss cone at $v_{||}>0$ (u).